nature neuroscience

Cortical gamma band synchronization through somatostatin interneurons

Julia Veit[1,2], Richard Hakim[1,2], Monika P Jadi[3,4], Terrence J Sejnowski[3,4] & Hillel Adesnik[1,2]

Gamma band rhythms may synchronize distributed cell assemblies to facilitate information transfer within and across brain areas, yet their underlying mechanisms remain hotly debated. Most circuit models postulate that soma-targeting parvalbumin-positive GABAergic neurons are the essential inhibitory neuron subtype necessary for gamma rhythms. Using cell-type-specific optogenetic manipulations in behaving animals, we show that dendrite-targeting somatostatin (SOM) interneurons are critical for a visually induced, context-dependent gamma rhythm in visual cortex. A computational model independently predicts that context-dependent gamma rhythms depend critically on SOM interneurons. Further *in vivo* experiments show that SOM neurons are required for long-distance coherence across the visual cortex. Taken together, these data establish an alternative mechanism for synchronizing distributed networks in visual cortex. By operating through dendritic and not just somatic inhibition, SOM-mediated oscillations may expand the computational power of gamma rhythms for optimizing the synthesis and storage of visual perceptions.

Rhythmic activity is a commonly observed feature of neuronal activity, from insects to primates, across a wide array of brain regions[1–4]. Although oscillatory synchronization, particularly in the gamma band, is thought to facilitate communication between phase-locked ensembles of excitatory neurons, its exact role, particularly in the cerebral cortex, remains a matter of debate[5–7]. Nevertheless, the underlying circuits that mediate gamma rhythmic entrainment are thought to depend on the reciprocal connection between excitatory neurons and local, soma-targeting parvalbumin (PV) inhibitory interneurons[8–11].

Gamma band rhythms in primary visual cortex have been particularly well studied in the context of visual processing[4], yet direct evidence for the circuits that mediate these rhythms is mostly lacking. For this reason, we leveraged optogenetic manipulations in awake, behaving mice, in addition to computational modeling, to address the cell types and circuit mechanisms of visually induced synchrony in the gamma band. We found that SOM neurons were intimately involved in a context-dependent visually induced gamma rhythm around 30 Hz, with their activity required to phase-lock cortical neurons to the ongoing oscillation. Notably, and consistent with their specific role in long range horizontal circuits in primary visual cortex (V1)[12], SOM neuron activity critically contributed to gamma coherence between coactive ensembles that encode widely separated regions of visual space. As SOM neurons primarily target the dendrites of cortical excitatory neurons, this implies that rhythmic dendritic inhibition represents an alternative mechanism for the generation or maintenance of gamma rhythms in the visual cortex.

RESULTS

We first explored cortical rhythmicity using multielectrode array recordings in layer 2/3 (L2/3) in V1 of awake, head-fixed but freely locomoting mice and collected both local field potentials (LFPs) and isolated single units. We presented full-contrast drifting gratings of multiple sizes and quantified power in different frequency bands of the LFP. As we increased the size of the visual stimulus we observed a large, nearly monotonic increase in power in a narrow band of the low gamma range (peak frequency at 21°: 32 ± 1 Hz, n = 32 mice; significant effect of stimulus size on gamma power $P < 0.001$, Kruskal-Wallis ANOVA; **Fig. 1a–c**). Importantly, many L2/3 units showed significant phase-locking to this visually induced oscillation (69 of 130 regular spiking (RS) units, 55.1%; 37 of 54 fast spiking (FS) 68.5%; stimulus size = 60°). At the same time, in most animals (25 of 30), we also observed a higher-frequency narrow gamma-band peak in the LFP (peak frequency, 60.7 ± 0.6 Hz; n = 32 mice; range, 53–66 Hz), which increased with the luminance of a uniform screen but was suppressed by drifting gratings of increasing size or contrast and was strongly modulated by behavioral state, consistent with prior studies (**Supplementary Fig. 1a–g**)[13,14]. We focus here exclusively on the size-dependent gamma oscillations typically found around 30 Hz.

Notably, the size-dependent increase in gamma synchronization in mouse V1 is also a reported feature of induced activity in awake, behaving monkeys[15,16] and humans[17], suggesting that it represents a fundamental and conserved feature of stimulus-driven V1 activity, even if the underlying center frequency varies between species. Furthermore, as in primates, in some mice (13 of 32) the peak frequency of the gamma oscillation also decreased monotonically with stimulus size (significant effect of size on peak frequency, $P = 0.014$; **Supplementary Fig. 1h,i**). While the visually induced gamma we observed in mice was found in the lower end of the 'typical' gamma spectrum[9,11,18], owing to its strong similarity to conventional visually induced gamma rhythms in alert primates, we call it 'gamma' and not 'beta', a 15- to 25-Hz rhythm often associated with movement control.

[1]Department of Molecular and Cell Biology, University of California, Berkeley, Berkeley, California, USA. [2]Helen Wills Neuroscience Institute, University of California, Berkeley, Berkeley, California, USA. [3]Howard Hughes Medical Institute, The Salk Institute for Biological Studies, La Jolla, California, USA. [4]Division of Biological Sciences, University of California at San Diego, La Jolla, California, USA. Correspondence should be addressed to H.A. (hadesnik@berkeley.edu).

Received 11 November 2016; accepted 18 April 2017; published online 8 May 2017; corrected online 16 June 2017 (details online); doi:10.1038/nn.4562

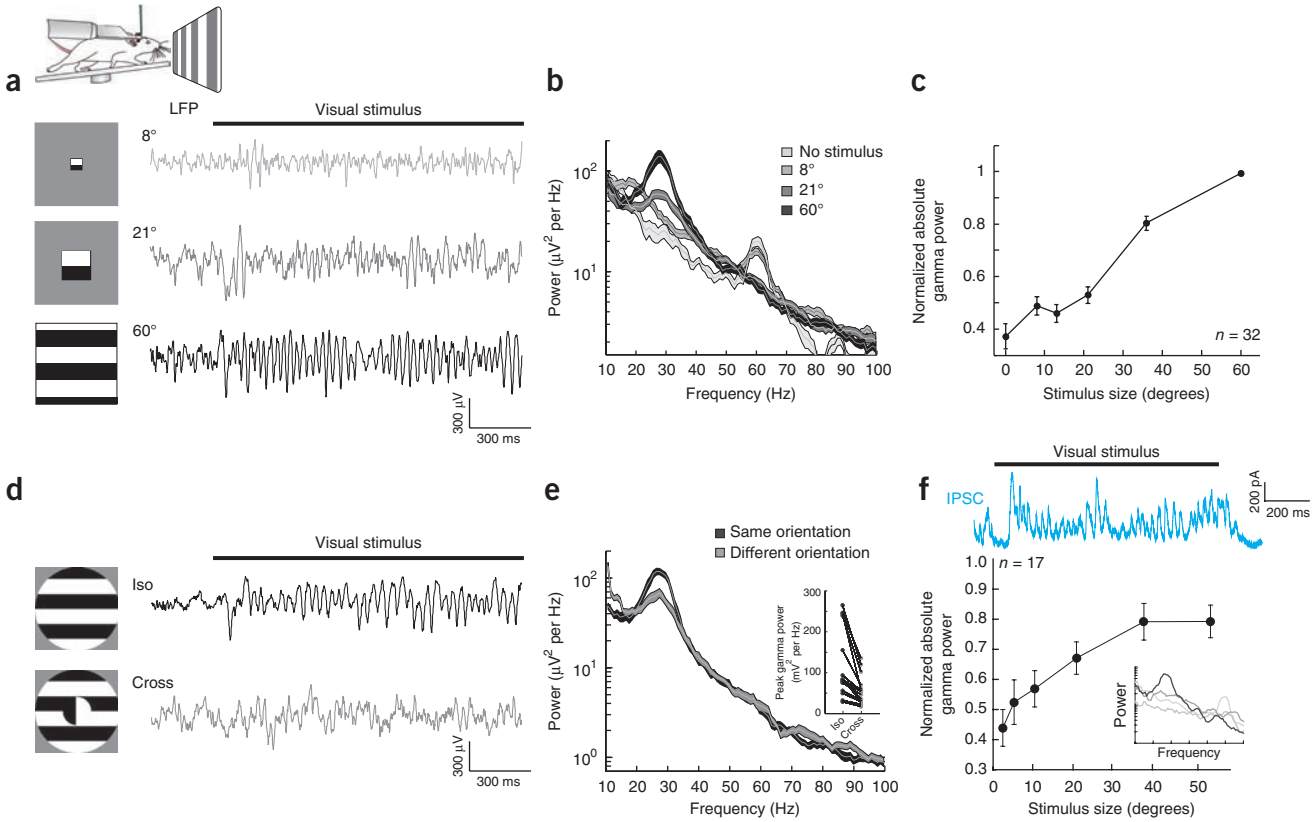

Figure 1 Visually induced gamma rhythms in V1 of the awake, running mouse are stimulus-dependent. (**a**) Top: experimental schematic of a head-fixed mouse on a running wheel facing a screen for visual stimulation. Bottom left: schematic of visual stimuli. Bottom right: example LFP traces in L2/3 of V1 while presenting drifting gratings of varying sizes. (**b**) Representative power spectra of the LFP for gratings of increasing size. Thickness of line denotes mean ± s.e.m. (**c**) Plot of normalized peak gamma power (peak frequency, 28 ± 1 Hz, $n = 32$ mice) vs. stimulus size ($P < 0.001$, Kruskal-Wallis ANOVA). (**d**) Left: schematic of iso-oriented and cross-oriented visual gratings. Right: example LFP traces for iso- and cross-oriented gratings. (**e**) Representative power spectra of the LFP to iso- and cross-orientated gratings. Inset: plot of peak gamma power between iso- and cross-oriented gratings ($n = 16$ mice, $P = 0.0004$, Wilcoxon signed-rank test). (**f**) Top: example voltage-clamped inhibitory postsynaptic current (IPSC) recorded in a L2/3 neuron during presentation of a 58° drifting grating. Bottom: plot of gamma power (30–40 Hz) vs. stimulus size ($n = 17$ cells, $P < 0.001$, Kruskal-Wallis ANOVA). Inset: example power spectra (PSD) of inhibitory postsynaptic currents at four increasing sizes (gray to black: 2.5°, 10°, 20° and 59°). Error bars in **c** and **f** denote s.e.m.

Moreover, since the peak frequency of visually induced gamma in primates spans a wide range depending on the size, contrast and the attention paid to the stimulus (from ~20 to > 60 Hz)[15,19,20], the gamma rhythm we observed in mice falls within the gamma spectrum delineated by many other studies.

Gamma rhythms have been linked to processing stimulus features that extend across large regions of the visual field[21]. Consistent with this notion, and as with prior reports in cats[22], the strength of the visually induced gamma rhythm depended on the match between stimulus features within and outside the classical receptive field (CRF) of the recording sites. If we rotated the orientation of the stimulus outside the CRF or offset its spatial phase relative to the stimulus presented inside the CRF, gamma power was substantially reduced (**Fig. 1d**,**e**; rotated surround, $n = 16$ mice; 49 ± 3% reduction, $P < 0.001$, signed-rank test; phase offset surround, $n = 11$ mice; 33 ± 3% reduction, $P < 0.001$, signed-rank test). This indicates that these gamma rhythms depend not only on the size but more generally on the spatial context of the visual stimuli that induce them. We thus refer to these visually induced oscillations as 'context-dependent gamma rhythms'.

What circuits mediate this visually induced, context-dependent gamma-band synchronization? Gamma oscillations in other brain areas are thought to be mediated by rhythmic inhibition to principal cells[8,9], and gamma in V1 correlates with subthreshold oscillations in the membrane potential[23,24]. To address whether inhibitory currents might underlie the visually induced gamma, we made intracellular patch-clamp recordings from V1 neurons in L2/3 in awake mice. We found prominent inhibitory currents with similar frequency and stimulus size-dependence in some of the recorded neurons (**Fig. 1f**; $n = 17$ cells). This indicates that the oscillations observed with extracellular recordings correlate well with gamma-paced inhibitory synaptic activity.

Next, we sought to dissect the differential contributions of cortical interneuron subtypes in generating the context-dependent gamma rhythm. Prevailing models of gamma-rhythm generation in the cortex implicate the action of soma-targeting PV neurons, yet to our knowledge none rely on the action of dendrite-targeting SOM neurons. However, the size-dependence of the visually induced gamma power mirrors the previously reported size-dependent increase in SOM neurons' firings rates[12], suggesting that SOM cells could be important. First, we quantified how well the firing of PV and SOM neurons (identified optogenetically; Online Methods) correlated with the visually induced gamma power. We found that PV and SOM cells phase-locked to the gamma rhythm equally well (pairwise phase consistency (PPC), an unbiased metric of oscillatory phase-locking: PV,

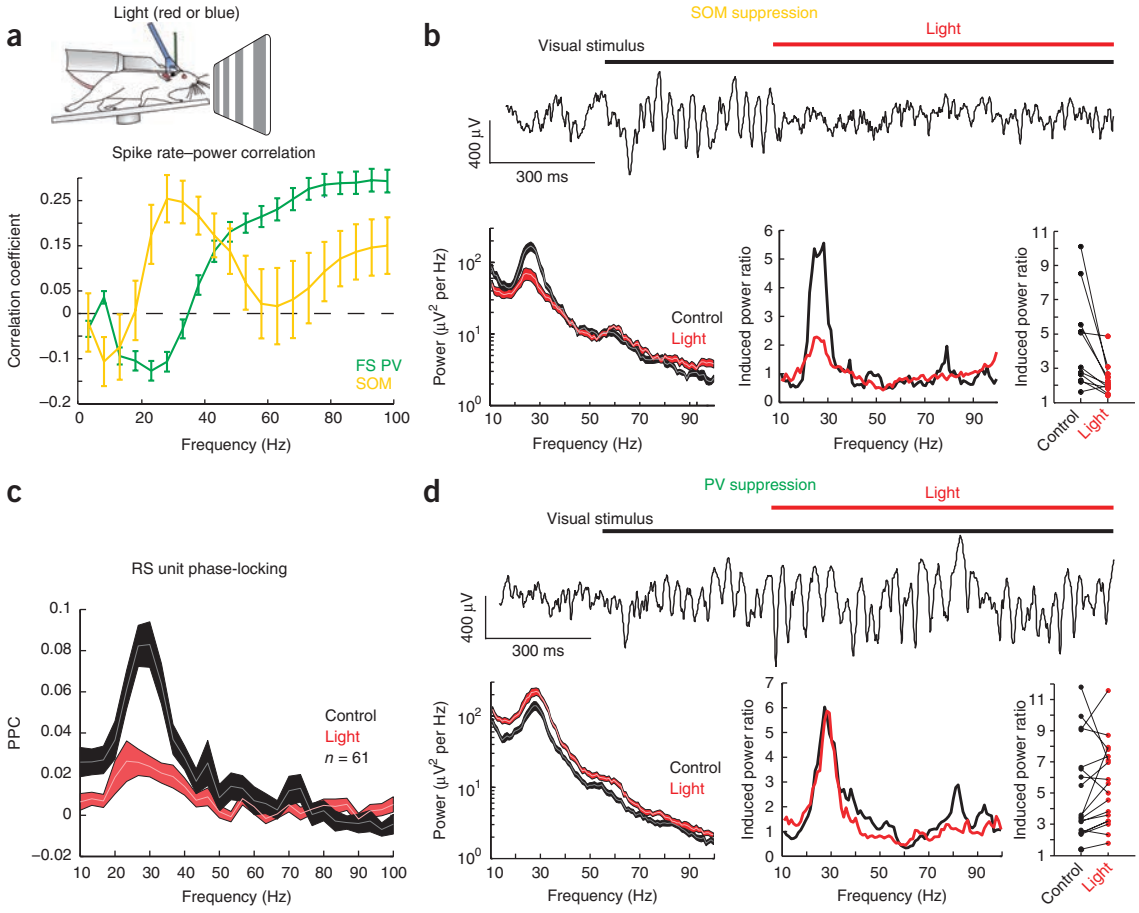

Figure 2 Cortical somatostatin interneurons are essential for visually induced gamma rhythms. (**a**) Top: schematic of a head-fixed mouse on a running wheel with an optical fiber placed close to the recording location. Bottom: average correlation between firing rate with spectral power for FS PV (green) and SOM (yellow) units. Error bars denote s.e.m.; the dashed line indicates zero correlation. (**b**) Top: example LFP trace from V1 of a SOM-Cre mouse during photosuppression of cortical SOM neurons. Left: representative power spectrum from V1 during visual stimulation with a large grating in the absence (black) and presence (red) of red light to suppress SOM neurons (thickness of line denotes mean ± s.e.m.). Middle: visually induced power spectrum for the same conditions (ratio of spectral response to grating compared to response to gray screen). Right: plot of the impact of light in SOM-Cre mice on induced gamma power ($n = 11$ mice, $P = 0.024$, Wilcoxon signed-rank test). (**c**) Average PPC spectrum for all L2/3 RS units in SOM-Cre mice in the absence (black) and presence (red) of light ($n = 61$ cells; thickness of line denotes mean ± s.e.m.). (**d**) As in **b** but for PV-Cre mice ($n = 18$ mice, $P = 0.17$, Wilcoxon signed-rank test).

0.10 ± 0.04, $n = 11$ cells; SOM, 0.09 ± 0.04, $n = 11$ cells, $P = 0.47$; rank-sum test), albeit to slightly different phases (**Supplementary Fig. 2**). On a trial-by-trial basis, however, PV neurons' firing rates were anti-correlated with spectral power in the context-dependent gamma band (−0.1 ± 0.02) and instead correlated more broadly with frequencies above 40 Hz (**Fig. 2a**). In contrast, SOM neurons' firing rates correlated strongly and specifically with the visually induced context-dependent rhythm around 30 Hz (0.2 ± 0.1; significantly different from PV, $P = 0.002$, rank-sum test; **Fig. 2a**). These findings, together with the size-dependent firing of SOM neurons, led us to hypothesize that SOM neurons may be critical for this lower-frequency, visually induced gamma oscillation.

To test this hypothesis, we suppressed SOM neurons with the optogenetic silencer eNpHR3.0, expressed using standard viral approaches (**Supplementary Fig. 3a** and Online Methods). Under our conditions, 89 ± 2% of SOM neurons in L2/3 expressed eNpHR3.0, and of 7 units we identified as putative SOM neurons (**Supplementary Fig. 3c** and Online Methods), we observed a 67 ± 8% reduction in their firing rate during illumination at the largest stimulus size. Unexpectedly, we found that even this partial suppression of SOM neurons strongly reduced the gamma power induced by large gratings in all 14 mice tested (**Fig. 2b**; induced gamma power (for calculation see Online Methods) control, 4.5 ± 0.8; light, 2.3 ± 0.3; $n = 11$ mice, $P = 0.003$, signed-rank test; for similar analyses see **Supplementary Fig. 3b**). The reduction in spectral power was also largely specific to the visually induced context-dependent gamma band (**Supplementary Fig. 3d**), with a tight correlation between the center frequency of the visual gamma peak and the center frequency of the reduction in spectral power ($r = 0.78$, $P < 0.001$; **Supplementary Fig. 3e**). At the same time, SOM suppression nearly abolished the phase-locking of L2/3 RS units as measured by the pairwise phase consistency (**Fig. 2c**; $n = 21$ of 61 significantly locked units; PPC control, 0.26 ± 0.03; PPC light, 0.06 ± 0.02; $P < 0.001$, signed-rank test). Notably, optogenetic suppression of SOM neurons also potently reduced the phase locking of FS units to the gamma rhythm (**Supplementary Fig. 3f**; $n = 17$ locked units; PPC control, 0.16 ± 0.03; PPC light, 0.05 ± 0.01, $P < 0.001$, signed-rank test). Since FS units often correspond to PV neurons, this demonstrates that SOM neuron activity was also crucial for the entrainment of putative PV neurons to the context-dependent gamma rhythm. Finally, we also tested whether suppressing SOM

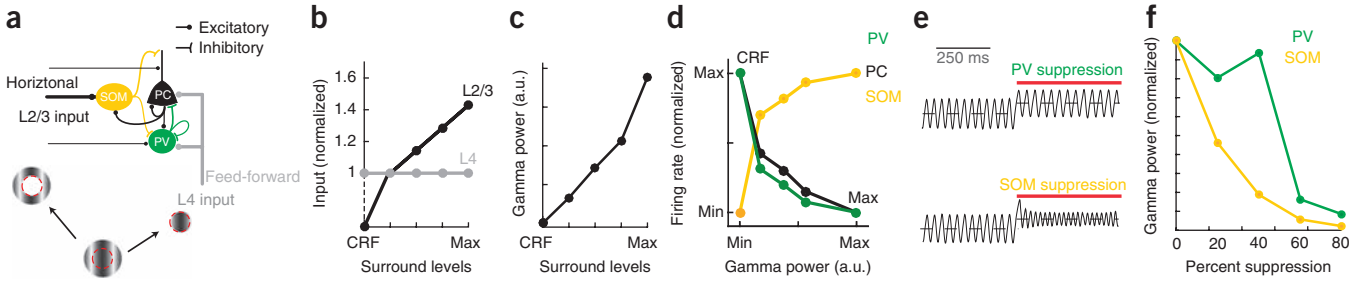

Figure 3 A computational model of visually induced gamma oscillations including both PV-type and SOM-type inhibitory neurons. (**a**) Schematic of the connectivity diagram for the computational model (see **Supplementary Fig. 5** for additional details). (**b**) Diagram of the total input to L2/3 PCs in the model from L4 and L2/3 as a function of increasing surround levels of input, analogous to visual stimuli of increasing size. The levels were varied from 1 to 4 to simulate increasing size of visual surround. (**c**) Plot of the gamma power of L2/3 PC activity as a function of surround levels. (**d**) Model prediction for the firing rate of PCs (black), PVs (green) and SOMs (yellow) as a function of total gamma power in the model. (**e**) Modeled plot of oscillatory firing rates of excitatory neurons during stimulation with large gratings during suppression of modeled PV (green) and SOM (yellow) type inhibitory neurons. (**f**) Model prediction for gamma power as a function of percentage silencing of modeled PV-type (green) and SOM-type (yellow) inhibitory neurons.

neurons even before the onset of the grating stimulus would reduce context-dependent gamma power and also found this to be the case (**Supplementary Fig. 3b**; mean reduction light after visual stimulus, 42.3 ± 7.4%; mean reduction light before visual stimulus, 29.9 ± 6.1%; $P = 0.1$, $n = 7$ mice, signed-rank test).

These findings demonstrate that SOM neurons are critical for the context-dependent gamma rhythm in V1 of awake mice. But what might the role of PV neurons be? To probe a causal relationship between PV neuron activity and context-dependent gamma oscillations, we optogenetically suppressed PV neurons (partial inactivation to avoid epileptiform activity; **Supplementary Fig. 4a** and Online Methods) and quantified the resulting effects on gamma power in response to large gratings. Of 11 FS units we could identify as putative opsin-expressing PV neurons through their strong suppression to light, we observed a net 66 ± 6% decrease in their firing rate (**Supplementary Fig. 4d**). *Post hoc* histology indicated that 88 ± 4% of PV neurons expressed the silencing opsin in L2/3 of V1. We found that suppressing PV neurons had no significant impact on the induced power in the context-dependent gamma band (control, 5.2 ± 0.7; light, 5.5 ± 0.6; $n = 18$ mice; $P = 0.17$, signed-rank test; **Fig. 2d**) and actually increased absolute spectral power across a broad frequency range (**Supplementary Fig. 4b**; absolute gamma power control, 170 ± 40 μV^2 per Hz; absolute gamma power light: 460 ± 130 μV^2 per Hz, $P < 0.001$, signed-rank test), even when optogenetic suppression preceded the visual stimulus (**Supplementary Fig. 4b**). PV suppression also slightly increased the phase-locking of L2/3 RS units to the context-dependent gamma band as measured by the spike PPC (47 of 105 significantly locked L2/3 RS cells; PPC control, 0.23 ± 0.03; PPC light, 0.3 ± 0.04; $n = 47$ cells; $P = 0.01$, signed rank test; **Supplementary Fig. 4c**). At the same time, we observed an increase in the mean firing rate of most isolated units, including some FS units that presumably did not express opsin, consistent with broad network disinhibition during PV neuron inactivation (RS, 134 ± 20% increase, $n = 145$ cells; nonsuppressed FS, 78 ± 21% increase, $n = 32$ cells; for optogenetic modulation index see **Supplementary Fig. 4f**).

To test how varying levels of optogenetic suppression of PV or SOM neurons influenced gamma power, we measured the impact of suppression on context-dependent gamma oscillations across a range of light intensities. While SOM suppression reduced gamma power at all levels of illumination, increasing light levels in PV-Cre mice drove further increases in total spectra power, consistent with the notion that PV neurons generally control cortical gain (**Supplementary Fig. 4g**,**h**). In a subset of animals, we tested even higher levels of PV-neuron suppression, but this often resulted in uncontrolled network activity, evidenced by ictal-like events in the LFP, precluding further quantitative analysis (**Supplementary Fig. 4j**,**k**). As a control for our optogenetic experiments, illuminating V1 in mice that were either not injected with any virus or injected with a virus driving only YFP expression had no effect on gamma power (**Supplementary Fig. 4i**).

To gain better mechanistic insight into the cortical generation of context-dependent gamma rhythms, we developed a computational model of upper layer V1 dynamics. This model builds on previous pyramidal–interneuron network for gamma (PING)[9] models of oscillations in Wilson-Cowan networks[25–27] that describe, using a single inhibitory cell type, the stimulus-size dependence of spectral gamma power in the visual cortex, as observed in primates[15] and here in mice. In a PING model, excitatory neurons drive inhibitory neurons, which provide recurrent inhibition back onto the excitatory population, thus driving an oscillation. Most PING models involve a single class of inhibitory neuron. Our model features two distinct inhibitory neuronal populations, solely constrained by the connectivity motifs of SOM and PV in the upper layer of V1 in mice[28] and their physiological responses to visual stimuli[12]. The two cell types in the model critically differ in terms of connectivity from outside the network: SOM neurons specifically integrate larger regions of visual space, through L2/3 horizontal projections, while PV neurons are preferentially driven by ascending projections from L4 (**Fig. 3a**,**b** and Online Methods). In this model, the power of size-dependent gamma critically depends on the size-dependent excitatory–inhibitory (E/I) balance at pyramidal cells. Because SOM cells are preferentially driven as stimulus size increases, SOM cells and not PV cells would be predicted to control the size-dependent change in E/I balance (see below). The model was not constrained by the experimental data presented above, to independently test if its predictions would be confirmed by physiological data.

We found that the model predicted many of the core experimental findings. First, we asked whether this model would recapitulate size-dependent gamma oscillations, and indeed, we found this to be the case (**Fig. 3c**). Next, we plotted the relationship the model predicts for the firing rates of the various neuronal subtypes with context-dependent gamma power. Consistent with the physiological data (**Fig. 2a**), the model predicts that SOM firing increases with gamma power, while that of pyramidal cells (PCs) and PVs decreases (**Fig. 3d**). Finally, we addressed how suppressing PV-type or SOM-type inhibitory neurons in the model influences context-dependent gamma power. The model predicts that suppression of SOM-type interneurons

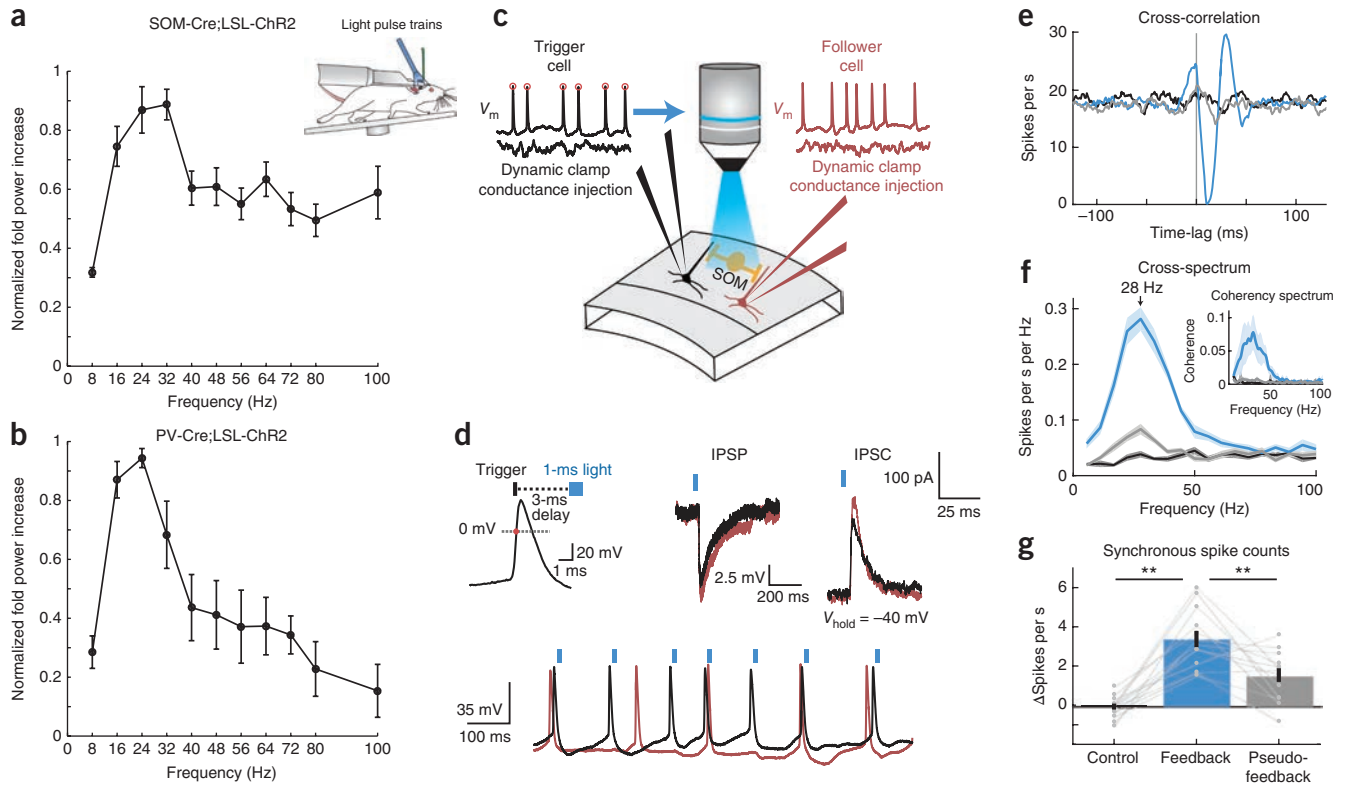

Figure 4 SOM neuron photostimulation can entrain gamma rhythmicity *in vivo* and *in vitro*. (**a**) Top: schematic of a head-fixed mouse with an optical fiber for delivering pulse trains. Bottom: plot of the normalized fold-increase in spectral power in different bands as a function of photostimulating SOM neurons at those frequencies ($n = 7$ cells; significant effect of stimulation frequency on fold-increase, $P < 0.001$, Kruskal-Wallis ANOVA). (**b**) As in **a** but for PV neurons ($n = 6$ cells; significant effect of stimulation frequency on fold-increase, $P = 0.013$, Kruskal-Wallis ANOVA). (**c**) Experimental schematic: two L2/3 PCs are patched in a slice from a mouse expressing ChR2 specifically in SOM neurons. The measured membrane potential is seen in the upper trace for both trigger and follower cell. PCs are injected with random and independent barrages of simulated excitatory conductances via a dynamic clamp (lower trace for both trigger and follower cells). A custom fast-feedback circuit detects rising 0 mV crossings of the membrane potential in the trigger cells (red circles in the voltage trace) and drives blue-light stimulation of nearby SOM-ChR2 neurons with a pulse of blue light. (**d**) Top left: schematic of the spike-triggered optical feedback scheme. Top middle: example membrane potential traces of the inhibitory postsynaptic potential (IPSP) recorded in a pair of PCs to a flash of blue light (peak IPSP amplitude population mean, 8.0 ± 0.9 mV). Current was injected to bring membrane potentials to –50mV. Top right: voltage-clamp recording from the same PC neurons to the same light stimulus; –40 mV holding potential (peak inhibitory postsynaptic current (IPSC) amplitude population mean, 210 ± 40 pA). Bottom: example traces of action potentials in the recorded pair (black, trigger cell; red, follower cell) while optical feedback was engaged. Blue ticks indicate flashes of blue light triggered by action potentials in the black trace. (**e**) Example cross-correlation between a recorded pair of PCs under control conditions (black), feedback (blue) and pseudofeedback (gray). (**f**) Average cross-spectrum between the two recorded neurons' spiking (mean values 22–39 Hz; control, 0.033 spikes per second per Hz; feedback, 0.242 spikes per second per Hz; pseudofeedback, 0.065 spikes per second per Hz; $P < 0.001$, Kruskal-Wallis ANOVA). Inset: average coherence spectrum. Shading in both plots denotes s.e.m. (**g**) Average changes in synchronous spike probability for the recorded pairs of neurons under control, feedback and pseudofeedback conditions (mean values: control = –0.001, feedback = 0.034, pseudofeedback = 0.015; $n = 13$ pairs; $^{**}P < 0.001$, Kruskal-Wallis ANOVA). All error bars denote s.e.m.

dramatically reduces gamma power, even for low levels of inactivation (**Fig. 3e**,**f**). This implies that SOM neurons are a crucial component of the inhibitory network for gamma generation in this PING model. In contrast, moderate suppression of PV-type interneurons (20–40%) has little to no effect on gamma power (**Fig. 3e**,**f**). Higher levels of PV neuron inactivation result in a dramatic increase of excitatory neuron activity (**Supplementary Fig. 5b**) and a drastic reduction in gamma power (**Fig. 3f**), suggesting that network stabilization via PV neurons is essential for gamma band oscillations, a prediction consistent with our physiological data, in which strong PV inactivation resulted in epileptiform activity (see above and **Supplementary Fig. 4j**,**k**).

Notably, the model also predicts that SOM suppression enhances both PC and PV firing rates, even as it potently reduces context-dependent gamma power (**Supplementary Fig. 5a**,**b**). This prediction is consistent with our physiological data; during SOM suppression, both L2/3 RS and FS cells significantly increased their firing rates (RS, 240 ± 50% increase, $n = 82$ cells; FS, 100 ± 30% increase, $n = 33$ cells; for optogenetic modulation index see **Supplementary Fig. 5c**,**d**). The increase in PV activity does not result in increases in gamma power, as might be assumed, because what drives gamma power in this model is not the increase in inhibition per se but the net E/I balance at PCs, which is under the control of both SOMs and PVs. The increase in PV cell activity in the model during SOM suppression is not due to direct disinhibition of PV cells, as it persists when the inhibitory connection from SOM to PV in the model is set to zero (**Supplementary Fig. 5e**,**f**). Instead, it can be explained by the increase of PC activity, which, in turn, increases PV neurons' firing rates (a typical consequence of the inhibition stabilized network; Online Methods). Broadly consistent with the extracellular data and the model, intracellular patch-clamp recording revealed that optogenetic SOM suppression also significantly

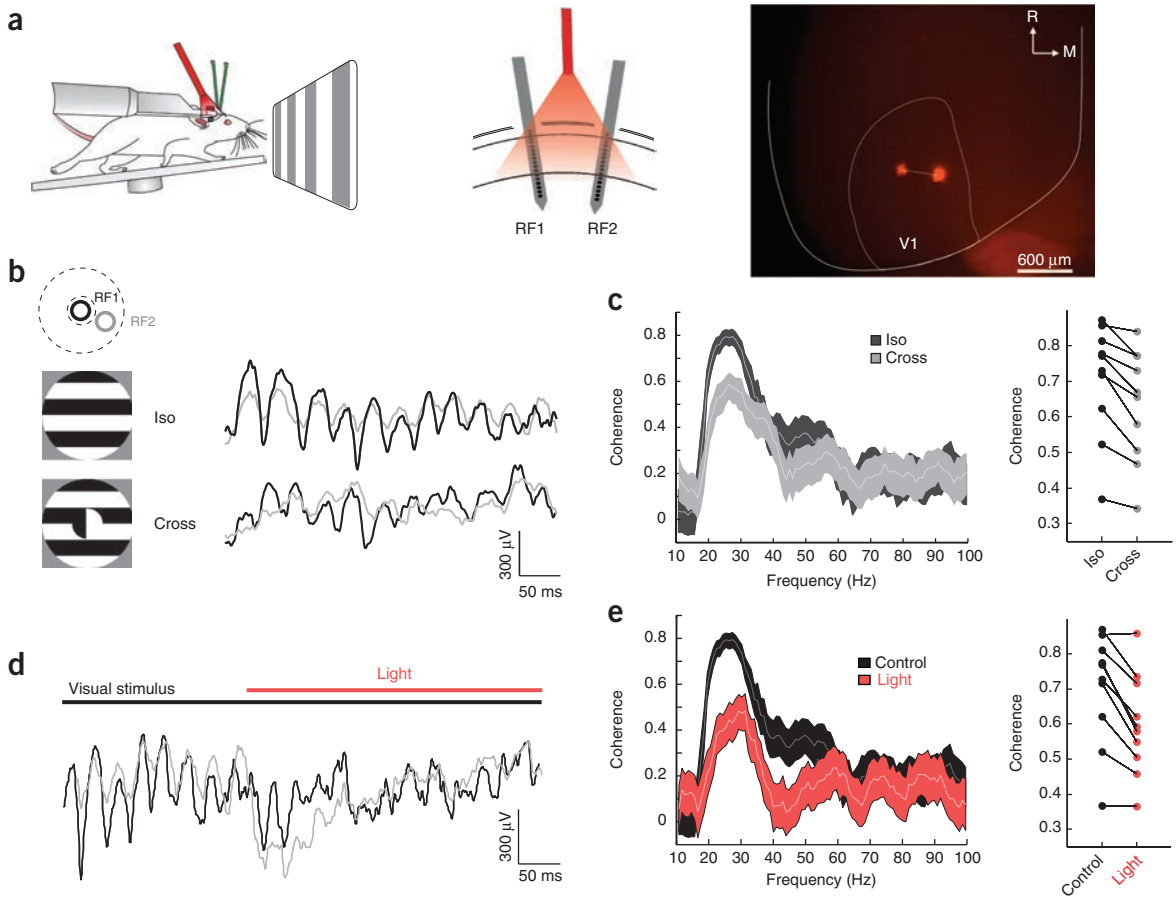

Figure 5 SOM interneurons synchronize distal ensembles in V1 of awake, behaving mice. (**a**) Left: recording schematic in awake, head-fixed SOM-Cre mice. Middle: schematic of the multielectrode array recording configuration with two laminar arrays in distant sites (610 ± 90 µm apart, histology from $n = 5$ mice) recorded from two separate receptive fields (RF1 and RF2, 18° ± 2° of visual angle separation, $n = 10$ mice). Right: example image from the brain of a SOM-Cre mouse showing two electrode tracks in V1. White lines show approximate outline of V1 in the left hemisphere. R, rostral; M, medial. (**b**) Left: schematic of the receptive fields' locations of the two laminar probes (top) and the large drifting gratings used to drive neural activity (bottom). The center and surround of the gratings are indicated with dashed lines in the top plot. Right: example simultaneously recorded LFP traces from the two electrodes (black, RF1; gray, RF2) during presentation of an iso-oriented surround grating (top) and a cross-oriented surround grating (bottom). (**c**) Left: example coherence spectra for simultaneously recorded LFP traces from the two laminar probes during iso-oriented (black) and cross-oriented gratings (gray). Thickness of line denotes 95% confidence intervals. Right: plot of the peak gamma coherence for iso- and cross-oriented gratings ($n = 10$ mice, $P = 0.002$; Wilcoxon signed-rank test). (**d**) Example LFP traces from two simultaneously recorded sites (black, RF1; gray, RF2) in V1 during photosuppression of SOM neurons while the mouse viewed the iso-oriented grating. (**e**) Left: Example coherence spectra between the two recorded sites for control (black) and SOM photosuppression (red) conditions. Thickness of line denotes 95% confidence intervals. Right: plot of peak gamma coherence between pairs of recording sites under control (black) and SOM photosuppression (red) conditions ($n = 10$ mice, $P = 0.002$; Wilcoxon signed-rank test).

reduced the relative gamma power of inhibitory postsynaptic currents ($n = 7$ cells, Friedman test; significant effect of light, $P = 0.022$; **Supplementary Fig. 5g**,**h**). Thus, even though this model was developed entirely independently of the physiological data presented above, it qualitatively predicts many of the physiological impacts of PV and SOM suppression on V1 dynamics. Taken together, the data and the model support the notion that SOM neurons are critical for these context-dependent gamma rhythms.

While these experiments indicate that SOM neuron activity is essential for context-dependent gamma band power, previous work has suggested that elevation of PV neuron activity, through optogenetic photostimulation, is sufficient to enhance gamma rhythms[11]. Our model predicts that gamma power correlates with the E/I balance in PCs. This means that photoactivating either interneuron subtype could, in principle, increase gamma power, so long as the net effect of the increase in their activity is a reduced E/I balance in PCs. Therefore, we tested whether SOM neuron photostimulation could also enhance gamma band power. Using SOM-Cre and PV-Cre mice crossed with the Cre-dependent channelrhodopsin 2 (ChR2) reporter mouse, Ai32, we asked how photostimulation of each interneuron subclass at different frequencies influenced spectral power in different bands, similarly to a previous approach[11]. We used glass electrodes to minimize photoelectric artifacts. Under these conditions, we found that driving both PV and SOM neurons was sufficient to increase spectral power, preferentially around 24–32 Hz, similar to the frequency of the context-dependent gamma rhythms (**Fig. 4a**,**b**; SOM-ChR2, 11 ± 2 fold increase, $n = 7$ mice; significant effect of stimulation frequency on fold-increase, $P < 0.001$, Kruskal-Wallis ANOVA; PV-ChR2, 28 ± 6 fold increase, $n = 6$ recordings in 4 mice; significant effect of stimulation frequency on fold-increase, $P = 0.013$, Kruskal-Wallis ANOVA). These data are consistent with model predictions and support the notion that activation of either inhibitory neuron subtype in

V1 is sufficient to enhance gamma band oscillations. It should be noted that the peak frequency of these light-induced rhythms in awake mice was lower than previously reported under anesthetized conditions in S1[11]. The difference in peak frequency is due to anesthesia (not brain area), as repeating the same experiments in S1 or V1 of anesthetized mice revealed a peak at ~48 Hz as previously reported (**Supplementary Fig. 6a**).

In many models of gamma rhythm generation, feedback inhibition from local interneurons is critical for pacing excitatory neuron activity. Previously, it has been shown that photostimulation of PV neurons in response to the activity of a single PC is sufficient to generate gamma rhythms[10]. Therefore, using a similar approach, we asked if photostimulating SOM neurons could also generate gamma rhythms. We built a feedback circuit in which the action potentials of a single PC triggered the photostimulation of ChR2-expressing SOM cells (**Fig. 4c**,**d**). We also patched a second PC to allow for coherence measurements between the two nearby excitatory neurons (<50 µm separation). Both PCs were driven to spike with random and independent barrages of excitatory conductances (Online Methods). When optical feedback was triggered off one cell's action potentials, we observed a dramatic and significant increase in the coherence, specifically in the gamma band, between the two recorded neurons' spiking (**Fig. 4e**,**f** and Online Methods; $P < 0.001$, Kruskal-Wallis ANOVA, $n = 13$), as well as a significant increase in synchronous spikes (Online Methods; $P < 0.001$, Kruskal-Wallis ANOVA, $n = 13$). As a control, we switched off the optical feedback and instead photostimulated SOM neurons with a light pulse train derived from randomly selected previous trials in which feedback was engaged ('pseudofeedback'). Despite photostimulating SOM neurons at essentially the same frequency, in the absence of true optical feedback, no increases in coherence or gamma rhythmicity were observed (**Fig. 4e–g**). These experiments indicate that SOM inhibition, in a recurrent circuit with excitatory neurons, is sufficient to generate and entrain gamma band rhythms and coherence between excitatory neurons.

What role might SOM-dependent gamma oscillations play in the spatial coding of visual stimuli? PCs in superficial cortical layers are well known to project long-range axons across the retinotopic map[29], which have been hypothesized to contribute to long-range synchronization[21]. To test this hypothesis we presented different types of drifting gratings to awake mice, covering the CRFs of two distinct V1 locations (~600 µm separation) targeted with independently movable laminar multielectrode arrays (**Fig. 5a**). By recording two sites in V1 simultaneously, we could measure both gamma power (as in **Fig. 1**) and the coherence of the gamma oscillations between the two distal sites. When the visual stimuli covering both receptive fields shared the same orientation and direction of motion, we observed a prominent peak in the LFP coherence in the context-dependent gamma band (**Fig. 5b**,**c**; $n = 10$ mice; iso-oriented, 0.56 ± 0.07; cross-oriented, 0.39 ± 0.05; $P = 0.002$, signed-rank test). We obtained identical results when we offset the center and surround in spatial phase and when we used side-by-side gratings of different orientations (data not shown). Optogenetic suppression of SOM neurons significantly reduced the LFP–LFP coherence between the two recording locations (**Fig. 5d**,**e**; control, 0.56 ± 0.7; light, 0.36 ± 0.06; $P = 0.002$, $n = 10$ mice). These data demonstrate that SOM neurons were essential for the long-range synchronization observed in the visual cortex during contextual stimulation.

DISCUSSION

This study demonstrates for the first time, to our knowledge, that a type of gamma rhythm critically depends on SOM interneurons. Although gamma-frequency oscillations in other cortical areas and brain regions[8–11], such as the hippocampus, and in higher spectral bands may depend primarily on PV neurons, context-dependent visually induced gamma activity in mouse V1 requires SOM neurons. PV neurons probably also contribute to these rhythms in V1, although our data more directly imply that they were necessary for stabilizing the cortical network and controlling cortical gain, consistent with prior findings[30,31]. Thus, one interpretation is that PV neurons provide the basis upon which SOM-mediated inhibition can then entrain gamma oscillations for large visual stimuli. Notably, a computational model built independently of this data predicted many of the key physiological findings in this study. This model provides quantitative insight and a future testing ground for further hypotheses concerning V1 gamma oscillations.

Previous studies using optogenetic manipulation of PV neurons[10,11] have demonstrated that altering their activity can influence or induce oscillations in the gamma range. We found that photostimulation of either inhibitory neuronal subtype was sufficient to enhance activity around 30 Hz in V1 of the awake mouse. This implies that there could be multiple circuit mechanisms for entraining gamma oscillations, which is potentially consistent with the heterogeneity of gamma oscillations observed in different cortical areas, brain states and frequency bands. A single brain area can exhibit distinct gamma rhythms[32] that might differentially depend on different neuronal sources of inhibition. In V1, we also observed a second prominent narrowband gamma rhythm around 55–65 Hz that was enhanced by luminance but suppressed by stimuli of increasing size and contrast, modulated by brain state and not reliant on SOM cell activity. Since this rhythm does not depend on contrast in the visual stimulus[14] and may arise in the retina[33–35], it is not clear what its specific role is in cortical processing. We do note that while locomotion and brain state are known to have profound effects on V1 activity[13,36], we did not observe any difference in the impacts of SOM or PV suppression on gamma power between quiescent and running conditions (**Supplementary Fig. 6b**,**c**).

A key finding in our data is that SOM-dependent oscillations specifically synchronized ensembles in V1 that were processing matched-stimulus features. This is consistent with a potential role for these long-range rhythms in linking disparate pieces of a sensory stimulus into a complete perception. However, several studies have called into question whether gamma rhythms do indeed contribute to feature-binding[37–39]. Although our data do not resolve this question directly, by revealing circuitry critically involved in long-range gamma synchronization, we have potentially enabled future studies to devise appropriate means to address this controversy.

What is the importance of gamma oscillations that depend on SOM neurons? By operating through dendritic inhibition, SOM-dependent gamma rhythms could provide much greater flexibility for influencing cortical computation and synaptic plasticity by interacting with specific dendritic compartments, perhaps on a gamma-cycle-by-gamma-cycle basis. A wealth of evidence indicates that dendrites can act as independent computational units by virtue of their ability to generate local spikes[40]. In V1, these local dendritic spikes have been implicated in improving feature coding[41], as well as in compartmentalizing information storage through dendrite-specific synaptic plasticity[42]. Since dendrite-targeting inhibitory neurons powerfully gate dendritic spiking and back-propagating action potentials[43], SOM-dependent gamma rhythms may enforce coordinated time windows for synaptic integration and spike-timing-dependent plasticity. Rhythmic inhibition of PC dendrites may thus provide a flexible means for binding distributed cell assembles in time to optimize information processing and storage. Indeed, a recent paper shows that dendrite-targeting

Martinotti cells in L5 could effectively synchronize thick-tufted L5 PC neurons in a frequency-dependent manner[44]. Since evidence suggests that SOM cells are involved in many aspects of V1 processing[12,31], their role in gating dendritic activation appears to be fundamental to sensory computation.

While our experiments have addressed SOM neurons' involvement in long-range gamma oscillations within the primary visual cortex, they also may play a key role in interareal gamma synchronization involved in higher cognitive processes. This is consistent with the fact that V1 SOM neurons have been shown to be among the targets of long-range, top-down input from higher cortical areas[45]. SOM neurons might also contribute to local gamma oscillations in other brain regions. For example, the neuropeptide somatostatin itself has been shown to be involved in gamma rhythms in the olfactory bulb[46]. Lastly, since some brain disorders, such as schizophrenia, have been linked to impaired gamma oscillations[47], it might be fruitful to explore whether defects in SOM cells and not just PV neurons might be relevant for the etiology of these diseases[48,49]. If SOM neurons are broadly involved in gamma rhythms beyond V1, future experiments may help explain why reductions in somatostatin and SOM interneurons are frequently associated with a host of neuropsychiatric diseases[50].

METHODS

Methods, including statements of data availability and any associated accession codes and references, are available in the online version of the paper.

Note: Any Supplementary Information and Source Data files are available in the online version of the paper.

ACKNOWLEDGMENTS

The authors thank D. Taylor for technical assistance, K. Chesnov and D. Abdelhalim for help with histology, and J. Isaacson, M. Feller, D. Feldman, Y. Dan and B. Atallah for comments on the manuscript. This work was supported by NEI grant R01EY023756-01. H.A. is a New York Stem Cell Foundation - Robertson Investigator. This work was supported by The New York Stem Cell Foundation. J.V. was supported by grants from the Swiss National Foundation (P300PA_164719 and P2FRP3_155172). M.P.J. was supported by NEI grant 5K99EY025026-02 and Howard Hughes Medical Institute (HHMI). T.J.S. was supported by HHMI.

AUTHOR CONTRIBUTIONS

H.A., J.V. and M.P.J. conceived of the study. J.V. performed all *in vivo* extracellular experiments; H.A. performed the *in vivo* patch-clamp experiments; and R.H. performed all brain slice experiments. M.P.J. conceived of the computational model and carried out all simulations. T.J.S. provided guidance to the computational study.

COMPETING FINANCIAL INTERESTS

The authors declare no competing financial interests.

1. Singer, W. & Gray, C.M. Visual feature integration and the temporal correlation hypothesis. *Annu. Rev. Neurosci.* **18**, 555–586 (1995).
2. Buzsáki, G. & Draguhn, A. Neuronal oscillations in cortical networks. *Science* **304**, 1926–1929 (2004).
3. Traub, R.D. & Whittington, M.A. *Cortical Oscillations in Health and Disease* (Oxford University Press, 2010).
4. Fries, P. Neuronal gamma-band synchronization as a fundamental process in cortical computation. *Annu. Rev. Neurosci.* **32**, 209–224 (2009).
5. Whittington, M.A., Cunningham, M.O., LeBeau, F.E.N., Racca, C. & Traub, R.D. Multiple origins of the cortical γ rhythm. *Dev. Neurobiol.* **71**, 92–106 (2011).
6. Fries, P., Nikolić, D. & Singer, W. The gamma cycle. *Trends Neurosci.* **30**, 309–316 (2007).
7. Womelsdorf, T. *et al.* Modulation of neuronal interactions through neuronal synchronization. *Science* **316**, 1609–1612 (2007).
8. Bartos, M., Vida, I. & Jonas, P. Synaptic mechanisms of synchronized gamma oscillations in inhibitory interneuron networks. *Nat. Rev. Neurosci.* **8**, 45–56 (2007).
9. Buzsáki, G. & Wang, X.J. Mechanisms of gamma oscillations. *Annu. Rev. Neurosci.* **35**, 203–225 (2012).
10. Sohal, V.S., Zhang, F., Yizhar, O. & Deisseroth, K. Parvalbumin neurons and gamma rhythms enhance cortical circuit performance. *Nature* **459**, 698–702 (2009).
11. Cardin, J.A. *et al.* Driving fast-spiking cells induces gamma rhythm and controls sensory responses. *Nature* **459**, 663–667 (2009).
12. Adesnik, H., Bruns, W., Taniguchi, H., Huang, Z.J. & Scanziani, M. A neural circuit for spatial summation in visual cortex. *Nature* **490**, 226–231 (2012).
13. Niell, C.M. & Stryker, M.P. Modulation of visual responses by behavioral state in mouse visual cortex. *Neuron* **65**, 472–479 (2010).
14. Saleem, A.B. *et al.* Subcortical source and modulation of the narrowband gamma oscillation in mouse visual cortex. *Neuron* **93**, 315–322 (2017).
15. Gieselmann, M.A. & Thiele, A. Comparison of spatial integration and surround suppression characteristics in spiking activity and the local field potential in macaque V1. *Eur. J. Neurosci.* **28**, 447–459 (2008).
16. Jia, X., Smith, M.A. & Kohn, A. Stimulus selectivity and spatial coherence of gamma components of the local field potential. *J. Neurosci.* **31**, 9390–9403 (2011).
17. Perry, G., Hamandi, K., Brindley, L.M., Muthukumaraswamy, S.D. & Singh, K.D. The properties of induced gamma oscillations in human visual cortex show individual variability in their dependence on stimulus size. *Neuroimage* **68**, 83–92 (2013).
18. Wang, X.J. & Buzsáki, G. Gamma oscillation by synaptic inhibition in a hippocampal interneuronal network model. *J. Neurosci.* **16**, 6402–6413 (1996).
19. Bosman, C.A. *et al.* Attentional stimulus selection through selective synchronization between monkey visual areas. *Neuron* **75**, 875–888 (2012).
20. Jia, X., Xing, D. & Kohn, A. No consistent relationship between gamma power and peak frequency in macaque primary visual cortex. *J. Neurosci.* **33**, 17–25 (2013).
21. Gray, C.M., König, P., Engel, A.K. & Singer, W. Oscillatory responses in cat visual cortex exhibit inter-columnar synchronization which reflects global stimulus properties. *Nature* **338**, 334–337 (1989).
22. Biederlack, J. *et al.* Brightness induction: rate enhancement and neuronal synchronization as complementary codes. *Neuron* **52**, 1073–1083 (2006).
23. Perrenoud, Q., Pennartz, C.M.A. & Gentet, L.J. Membrane potential dynamics of spontaneous and visually evoked gamma activity in V1 of awake mice. *PLoS Biol.* **14**, e1002383 (2016).
24. Jagadeesh, B., Gray, C.M. & Ferster, D. Visually evoked oscillations of membrane potential in cells of cat visual cortex. *Science* **257**, 552–554 (1992).
25. Wilson, H.R. & Cowan, J.D. Excitatory and inhibitory interactions in localized populations of model neurons. *Biophys. J.* **12**, 1–24 (1972).
26. Jadi, M.P. & Sejnowski, T.J. Cortical oscillations arise from contextual interactions that regulate sparse coding. *Proc. Natl. Acad. Sci. USA* **111**, 6780–6785 (2014).
27. Jadi, M.P. & Sejnowski, T.J. Regulating cortical oscillations in an inhibition-stabilized network. *Proc. IEEE Inst. Electr. Electron. Eng.* **102**, http://dx.doi.org/10.1109/JPROC.2014.2313113 (2014).
28. Pfeffer, C.K., Xue, M., He, M., Huang, Z.J. & Scanziani, M. Inhibition of inhibition in visual cortex: the logic of connections between molecularly distinct interneurons. *Nat. Neurosci.* **16**, 1068–1076 (2013).
29. Gilbert, C.D. & Wiesel, T.N. Columnar specificity of intrinsic horizontal and corticocortical connections in cat visual cortex. *J. Neurosci.* **9**, 2432–2442 (1989).
30. Atallah, B.V., Bruns, W., Carandini, M. & Scanziani, M. Parvalbumin-expressing interneurons linearly transform cortical responses to visual stimuli. *Neuron* **73**, 159–170 (2012).
31. Wilson, N.R., Runyan, C.A., Wang, F.L. & Sur, M. Division and subtraction by distinct cortical inhibitory networks in vivo. *Nature* **488**, 343–348 (2012).
32. Colgin, L.L. *et al.* Frequency of gamma oscillations routes flow of information in the hippocampus. *Nature* **462**, 353–357 (2009).
33. Neuenschwander, S. & Singer, W. Long-range synchronization of oscillatory light responses in the cat retina and lateral geniculate nucleus. *Nature* **379**, 728–732 (1996).
34. Koepsell, K. *et al.* Retinal oscillations carry visual information to cortex. *Front. Syst. Neurosci.* **3**, 4 (2009).
35. Storchi, R. *et al.* Modulation of fast narrowband oscillations in the mouse retina and dLGN according to background light intensity. *Neuron* **93**, 299–307 (2017).
36. Vinck, M., Batista-Brito, R., Knoblich, U. & Cardin, J.A. Arousal and locomotion make distinct contributions to cortical activity patterns and visual encoding. *Neuron* **86**, 740–754 (2015).
37. Ray, S. & Maunsell, J.H.R. Differences in gamma frequencies across visual cortex restrict their possible use in computation. *Neuron* **67**, 885–896 (2010).
38. Thiele, A. & Stoner, G. Neuronal synchrony does not correlate with motion coherence in cortical area MT. *Nature* **421**, 366–370 (2003).
39. Shadlen, M.N. & Movshon, J.A. Synchrony unbound: a critical evaluation of the temporal binding hypothesis. *Neuron* **24**, 67–77, 111–125 (1999).
40. Larkum, M.E., Nevian, T., Sandler, M., Polsky, A. & Schiller, J. Synaptic integration in tuft dendrites of layer 5 pyramidal neurons: a new unifying principle. *Science* **325**, 756–760 (2009).
41. Smith, S.L., Smith, I.T., Branco, T. & Häusser, M. Dendritic spikes enhance stimulus selectivity in cortical neurons in vivo. *Nature* **503**, 115–120 (2013).
42. Losonczy, A., Makara, J.K. & Magee, J.C. Compartmentalized dendritic plasticity and input feature storage in neurons. *Nature* **452**, 436–441 (2008).

43. Murayama, M. *et al*. Dendritic encoding of sensory stimuli controlled by deep cortical interneurons. *Nature* **457**, 1137–1141 (2009).
44. Hilscher, M.M. *et al*. Chrna2-Martinotti cells synchronize layer 5 type A pyramidal cells via rebound excitation. *PLoS Biology* **15**, e2001392 (2017).
45. Zhang, S. *et al*. Selective attention. Long-range and local circuits for top-down modulation of visual cortex processing. *Science* **345**, 660–665 (2014).
46. Lepousez, G., Mouret, A., Loudes, C., Epelbaum, J. & Viollet, C. Somatostatin contributes to in vivo gamma oscillation modulation and odor discrimination in the olfactory bulb. *J. Neurosci.* **30**, 870–875 (2010).
47. Uhlhaas, P.J. & Singer, W. Abnormal neural oscillations and synchrony in schizophrenia. *Nat. Rev. Neurosci.* **11**, 100–113 10 (2010).
48. Jadi, M.P., Behrens, M.M. & Sejnowski, T.J. Abnormal gamma oscillations in N-methyl-D-aspartate receptor hypofunction models of schizophrenia. *Biol. Psychiatry* **79**, 716–726 (2016).
49. Hamm, J.P. & Yuste, R. Somatostatin interneurons control a key component of mismatch negativity in mouse visual cortex. *Cell Rep.* **16**, 597–604 (2016).
50. Lin, L.C. & Sibille, E. Reduced brain somatostatin in mood disorders: a common pathophysiological substrate and drug target? *Front. Pharmacol.* **4**, 110 (2013).

ONLINE METHODS

Transgenic mice. All experiments were performed in accordance with the guidelines and regulations of the ACUC of the University of California, Berkeley. Mice for the *in vivo* experiments were housed in groups of five or less with a 12:12-h light:dark cycle. Both female and male mice were used. Experiments *in vivo* were performed on animals aged 7–20 weeks during their subjective night. *In vitro* experiments were performed on animals aged P19–P23. We used PV-Cre (JAX stock 008069), SOM-IRES-Cre (JAX stock 013044), AI32 (JAX stock 012569) and Rosa-LSL-tdTomato (JAX stock 007909) mice. Mice were out-crossed for one generation to the ICR white strain (Charles River). The numbers of animals used were not predetermined for a specified effect size.

Viral infection. Neonatal SOM and PV-Cre mice (P3–P6) were briefly cryoanesthetized and placed in a head mold. We injected ~45 nl of undiluted AAV9-EF1a-DIO-eNpHR3.0-YFP or AAV9-DIO-ChR2 (UPenn Vector Core; SOM-Cre: 20 animals; PV-Cre: 12 animals, ChR2: SOM-Cre: 3 animals; PV-Cre: 3 animals) using a Drummond Nanoject injector at three locations in V1 using a glass pipette beveled to fine tip (~30–60 μm). With respect to the lambda suture, coordinates for V1 were +0.0 mm AP and +2.2 mm L, and injections were given as superficially as possible under the skull. AAV-EF1a-DIO-eArch3.0-YFP (UNC vector core, 7 animals) injections were performed on PV-Cre animals 3–6 weeks old. Mice were anesthetized with isoflurane (2.5% vapor concentration), and ~500 nL of undiluted virus was injected through a burr hole 3 mm lateral of lambda, ~400–600 μm deep.

Preparation for *in vivo* recording. Mice were anesthetized with isoflurane (2.5% vapor concentration). The scalp was removed, the fascia retracted and the skull lightly etched with a 27 gauge needle. Following application of Vetbond to the skull surface, a custom stainless steel headplate was fixed to the skull with dental cement (Metabond). Mice were allowed to recover from surgery for at least 2 d. Then mice were habituated to head-fixation on a free-spinning circular treadmill for 2–10 d. On the day of recording, mice were briefly anesthetized with isoflurane (2%), the skull over V1 was thinned and one or two (spacing 400–1,000 μm) small (< 250 μm) craniotomies were opened over V1 with a fine needle.

Visual stimulation. Visual stimuli were generated with Psychophysics Toolbox[51] running on an Apple Mac Mini and were presented on a gamma-corrected 23-inch Eizo FORIS FS2333 LCD display with a 60-Hz refresh rate. At the beginning of each recording session, the receptive fields of MUA recorded at each cortical location were mapped with sparse noise to enable us to precisely position the grating stimuli. The stimulus was centered on a location where a small grating, movable by hand, elicited a clear response. Sparse noise consisted of black and white squares (2 visual degrees, 80 ms) on a 20 × 20 visual degree grid flashed onto a gray background of intermediate luminance. To improve receptive field estimation, the same stimulus grid was offset by 1° and the resulting maps were averaged. MUA average receptive fields were calculated online by reverse correlation. Visual stimuli consisted of full-contrast drifting square-wave gratings at 0.04 cycles per degree and 2 cycles s^{-1} centered on the average MUA receptive field. Gratings were presented in two different configurations: (i) square-wave gratings of eight different directions (0–315° in steps of 45°) and five different sizes (8, 13, 21, 36 and, if possible, 60 visual degrees; if the RF was not perfectly centered on the monitor, the effective largest size was slightly smaller; see **Fig. 1a**); (ii) square-wave gratings with a circular aperture 12 visual degrees in diameter, centered on the MUA receptive field of one of the two simultaneously recorded cortical locations, surrounded by a 60° grating of either the same orientation, the orthogonal orientation or the same orientation, offset by 180° of phase. For the coherence analysis, we only analyzed cases in which the second receptive field was covered entirely and exclusively by the surround-stimulus (**Figs. 1d** and **4b**). For the contrast-dependence of the high-gamma rhythm, we also presented small (12°) gratings centered on the MUA receptive field at varying contrasts levels (0, 0.1, 0.18, 0.32, 0.56 and 1.0 Michelson contrast). Temporal and spatial frequencies, as well as presentation time, were the same as above. In a subset of animals, we also showed an isoluminant screen without contrast and varied the luminance in five steps between 0 and 1.

Optogenetic stimulation *in vivo*. For optogenetic stimulation of eNpHR3.0 *in vivo*, we used red (center wavelength: 640 nm, 3–30 mW for the dose response curve in **Supplementary Fig. 4f**,**g**); for stimulation of eArch3.0 we used green light (center wavelength: 550 nm, 0.3–12 mW) from the end of a 1-mm diameter multimode optical fiber coupled to a solid-state source (Lumencor Spectra X); and for stimulation of ChR2 we used blue light (center wavelength: 455 nm, 0.5–3 mW) from a fiber-coupled LED (Thorlabs) controlled by digital outputs (NI PCIe-6353). The fiber was placed as close to the craniotomy as possible (< 3 mm). The illumination area was set to illuminate a wide area including all of V1. Light levels were tested in increasing intensities at the beginning of the experiment and were kept at the lowest possible level that still evoked observable change in ongoing activity for the remainder of the recording. In the eArch3.0 injected PV-Cre mice, very low intensities of light (~0.3 mW) evoked substantial changes in ongoing activity, and when the light intensity was increased beyond 5–12 mW ictal/epileptiform activity was typically observed. In these cases, the light was kept at a level that did not induce epileptiform activity, and, if necessary, the optic fiber was moved slightly farther from the craniotomy. We only used viral injections into V1 and did not attempt to use an Arch or eNphR transgenic reporter line, to avoid off-target expression of the opsin and nonspecific optogenetic suppression of subcortical nuclei (such as the thalamic reticular nucleus) that are also labeled in the PV-Cre line.

Gratings drifted for 2 s with 1-s intertrial intervals, with the red or green LED switched on for 1 s starting 0.5 s after start of the visual stimulus in 50% of the trials. The period of light was chosen to influence the stable steady-state of the response to the grating, and all analysis was performed during this time window. For a subset of animals (n = 7 for SOM mice and n = 8 for PV mice) we ran a separate experiment in which only large, full-contrast gratings were presented and the light was turned on 500 ms before the onset of the 2-s grating in 50% of the trials. In this case, analysis was performed on a 1-s window immediately after grating onset. For optogenetic identification of SOM cells the cortex was illuminated by low intensity blue-light ramps or by pulse-trains during the same light window for the same stimulus set as for the eNpHR experiments.

***In vivo* extracellular multielectrode electrophysiology.** One or two 16-channel linear electrodes with 25-μm spacing (NeuroNexus, A1x16-5mm-25-177-A16) were guided into the brain using micromanipulators (Sensapex) and a stereomicroscope (Leica). Electrical activity was amplified and digitized at 30 kHz (Spike Gadgets) and stored on a computer hard drive. The cortical depth of each electrical contact was determined by zeroing the bottom contact to the surface of the brain. Electrodes were inserted nearly perpendicular to the brain's surface for single electrode recordings and ~25° from vertical for the two electrode experiments. After each recording a laminar probe coated with the lipophilic dye DiI was used to mark each electrode track to quantitatively assess its insertion angle and depth with *post hoc* histologic reconstructions. The laminar depth of recorded units was corrected for the insertion angle and the local curvature of the neocortex.

Analysis of local field potential data. All analysis was performed using custom-written code or freely available packages in Matlab (Mathworks). Local field potentials were extracted by low-pass filtering the raw signal (sampled at 30 kHz) below 200 Hz and subsequently down-sampling to 1 kHz. For LFP-only analysis we always analyzed the LFP from the electrode contact closest to a cortical depth of ~330 μm (in cortical layer 3). For spike-locking to the LFP, we used the LFP from an electrode contact 50 μm away from the contact with the largest spike-waveform amplitude to reduce contamination of the LFP.

The power spectrum was computed in a 800-ms analysis window starting 200 ms after light onset (to exclude any photoelectric artifacts sometimes present in the first ~150 ms after light onset) using multitaper estimation in Matlab with the Chronux package (http://chronux.org/)[52] using three tapers. All analysis was performed on the power at the peak of each animal's specific gamma oscillation. Peaks were identified as local maxima on the smoothed spectrum, between 20 and 40 Hz for the low-gamma peak and between 50 and 70 Hz for the high-gamma peak, that were preceded by local minima in the 15 Hz preceding the peak. For the high-gamma peak, two animals were excluded because of visible line noise in the recording that would have precluded proper analysis. Thus, 25/30 animals had distinguishable high-gamma peaks for the smallest stimulus size and all 32/32 animals had visual gamma peaks for the largest stimulus size. Visually induced spectra were calculated by dividing the spectrum for the largest grating size by the spectrum for a plain gray screen. Relative gamma power was calculated

doi:10.1038/nn.4562

as the peak gamma power divided by the average spectral power between 10 and 100 Hz. The peak/trough ratio was estimated as power at the peak divided by the power of the preceding trough.

For calculation of coherence, bipolar derivatives of the LFP were calculated by subtracting the electrode channel immediately above the channel of interest to remove the common recording reference and to enhance spatial specificity of the signal. Coherence between the sites was determined using the Chronux package with the same number of tapers as the power analysis. All spectral plots show mean ± s.e.m.; the coherence spectra show jack-knifed 95% confidence intervals.

In $n = 7$ SOM Ai32 mice (7 sites total) and $n = 4$ PV Ai32 mice (6 sites total) we stimulated V1 in the awake condition with 3-s bouts of 11 different frequencies of blue-light pulses (3-ms pulse duration) from 8 to 100 Hz (8, 16, 24, 32, 40, 48, 56, 64, 72, 80 and 100 Hz); and under control conditions (no stimulation), similar to a previous study in anesthetized barrel cortex[11]. We recorded 30 repetitions per stimulation frequency for 2–4 different light intensities between 0.1 and 4.1 mW for each animal. For these experiments, the LFPwas recorded with low-resistance borosilicate pipettes to avoid a direct optoelectric artifact from the stimulating light on the silicon electrodes. Resulting LFP traces were mean-subtracted and frequency-transformed (as above), and the resulting spectra were averaged over the 30 trials for each frequency. For analysis we chose the lowest light intensity for each animal that produced reliable peaks higher than the control spectrum for all stimulation frequencies. For each stimulation frequency, we calculated the ratio of the power at the stimulation frequency to the power at the same frequency under control conditions. We repeated this experiment in PV-Cre mice injected as adults with AAV9-DIO-ChR2-YFP in V1 ($n = 4$ mice) and S1 ($n = 3$ mice) and anesthetized with isoflurane (2.5% vapor concentration).

Analysis of spiking data. Spiking activity was extracted by filtering the raw signal between 800 and 7,000 Hz. Spike detection was performed using the UltraMega Sort package[53]. Detected spike waveforms were sorted using the MClust package (http://redishlab.neuroscience.umn.edu/MClust/MClust.html). Waveforms were first clustered automatically using KlustaKwik and then manually corrected to meet criteria for further analysis. With the exception of two burst-firing units, included units had no more than 1.5% of their individual waveforms violating a refractory period of 2 ms. Individual units were classified as either fast-spiking or regular spiking using a *k*-means cluster analysis of spike waveform components. Since the best separation criterion was the trough-to-peak latency of the large negative-going deflection and clustering is nondeterministic, we defined all units with latencies shorter than 0.36 ms as fast-spiking and all units with latencies larger than 0.38 ms as regular-spiking. Cells with intermediate latencies were excluded from further analysis. Putative eNpHR3.0- or eArch3.0-expressing cells were identified by significantly reduced firing rates during the red-light illumination period. Putative ChR2-expressing cells were identified by dramatic increases in spike rates to blue-light stimulation. For PV cells, the spike waveform had to be additionally classified as FS as described above. For SOM cells, three additional criteria suggested they were in fact SOM cells: all waveforms were of intermediate spike width (0.37–0.44 ms)[54], preferred either the largest or second-largest stimulus[12] and often exhibited a rebound spike after light offset, consistent with their known physiological properties[55]. Data from PV-Cre mice injected with either eNpHR3.0 or eArch3.0 were not significantly different and so were combined (fold power change: Halo, 2.19 ± 0.19; eArch, 2.22 ± 0.30; $P = 0.97$, Wilcoxon rank-sum test). Identified PV and SOM neurons were grouped with the eNpHR3.0-identified neurons for phase locking and gamma power correlation analyses. Because we found no differences between the identified PV cell group and the FS group, these were merged for these analyses as well.

The depth of each unit was assigned based on the calculated depth of the electrode on the array that exhibited its largest amplitude-sorted waveform. Layer boundaries were determined following a previously established approach[56]. Firing rates were computed from counting spikes in a 1-s window starting 500 ms after the onset of the visual stimulus, which coincided with the onset of the LED during optogenetic suppression trials. Unless otherwise stated, we only analyzed trials when the animal was moving (at least 1cm/s) and not accelerating or decelerating abruptly (not more than 1.5 s.d. deviation from the animal's mean running speed). However, we observed the same effects of SOM and PV neuron suppression when the animal was not running (**Supplementary Fig. 6b,c**). Average running speed across the population was 41 ± 25 cm/s ($n = 20$ animals). Two animals were excluded because they ran fewer than 15% of total trials.

For the correlation of spike rate and LFP power, the LFP was filtered into 20 non-overlapping narrow frequency bands (5 Hz each) and the power in each trial was estimated using the Hilbert transform. The average power in each band was then correlated with the spike rate of the neuron on a trial-by-trial basis using Spearman's rank correlation.

To quantify locking of spiking activity to the gamma band, we bandpass-filtered the LFP in a 20-Hz band around the peak and extracted the oscillation's instantaneous phase by using the imaginary part of the analytical signal using the Hilbert transform. Each spike was thus assigned an exact phase in the gamma oscillation. Phase-locking magnitudes were determined for each unit by the pairwise phase consistency (PPC), a measure of synchrony that is not biased by the number of spikes[57]; results were similar when quantifying phase-locking strength by the resultant vector length (phase-locking value; data not shown). The significance of locking was determined by the Rayleigh test for nonuniformity on the distribution of spike-phases. All units with $P < 0.05$ were considered to be significantly locked. We only included units that fired more than 10 spikes total in response to the largest grating size in the control condition. PPC spectra were calculated from the spike-triggered LFP spectrum for each unit using the FieldTrip Matlab package[58].

Optogenetic modulation index (OMI) was calculated as

$$R_l - R_c \Big/ R_l + R_c$$

where R_l is the average firing rate of the neuron in the light period and R_c is the average firing rate of the neuron in the control condition.

***In vivo* intracellular recording and analysis.** Mice were prepared identically as for extracellular recording. For blind whole-cell patch-clamp recordings, a glass borosilicate pipette (Sutter) was pulled to a long taper and a low resistance (3–5 MΩ) and inserted axially through the dura mater under high positive pressure. The electrode solution was the same as for brain-slice recordings for voltage clamping (see below; solution contained cesium, QX-314 and TEA). Signals were amplified with an Axopatch 200B (Molecular Devices), filtered at 2 kHz and digitized with a National Instruments DAQ device (PCIe-6323). The depth of the electrode was set to zero when the pipette encountered the dural surface, which was easily identified electrically by a large, transient increase in pipette resistance. The pipette was then advanced to L2/3 (~100–350 μm below the dura; mean cell depth, 250 ± 20 μm) under high pressure (~180 mbar). The pipette was advanced in 2-μm steps, and following a sudden and transient increase in pipette resistance, the positive pressure was released. Following gigaseal formation, brief suction ruptured the membrane, providing whole-cell access. The cell was dialyzed 5–10 min before voltage clamping to the reversal potential of synaptic excitation, to isolate inhibitory conductances. Gamma power (25–40 Hz) was measured in power spectra of the averages of IPSCs recorded across different stimulus sizes. Relative gamma power was computed as the ratio between power from 25–40 Hz and power between 50–70 Hz.

Brain slice preparation. Cortical slices containing primary visual cortex were cut in the coronal plane (400-μm thick) were prepared from mice aged P19–P23, using a DSK Microslicer in a reduced sodium solution containing (in mM) 83 NaCl, 2.5 KCl, 3.3 $MgSO_4$, 1 NaH_2PO_4, 22 glucose, 72 sucrose and 0.5 $CaCl_2$. It was stored submerged at 34 °C for 30 min, then at room temperature for 1–5 h in the same solution before being transferred to a submerged recording chamber maintained at 31–32 °C by inline heating in a solution containing (in mM) 119 NaCl, 2.5 KCl, 1.3 $MgSO_4$, 1.3 NaH_2PO_4, 20 glucose, 26 $NaHCO_3$ and 2.5 $CaCl_2$. Before the beginning of the recordings, all slices were inspected with epifluorescence to ascertain the location and quality of transfection.

Whole-cell recordings *in vitro*. Whole-cell recordings were performed using glass micropipettes (resistance 2–3 MΩ) pulled on a Sutter P-1000 Micropipette Puller. For voltage-clamp recordings, pipettes were filled with a Cs^+-based internal solution containing, in mM: 135 $CsMeSO_4$, 8 NaCl, 10 HEPES, 0.3 Na_3GTP, 4 MgATP, 0.3 EGTA, 5 QX-314-Cl and 5 TEA-Cl. For current-clamp recordings,

pipettes were filled with a potassium-gluconate based internal solution containing (in mM): 135 potassium-gluconate, 8 NaCl, 10 HEPES, 0.3 Na_3GTP, 4 MgATP and 0.3 EGTA. Voltage-clamp recordings were not corrected for the liquid junction potential. Series resistance was not compensated for, but we monitored it continuously with negative voltage steps. Data were analyzed from recordings in which series resistance was below 25 MΩ and did not change by more than 30% during the course of the experiment. Data were acquired and filtered at 2 kHz using a Multiclamp 700B Amplifier (Axon Instruments) and digitized at 20 kHz (National Instruments). All data were acquired using custom written Matlab (Mathworks) software. Excitatory and inhibitory currents were isolated by voltage-clamping the neuron at the reversal potential for synaptic inhibition and excitation respectively. For cell-attached experiments, only cells that exhibited at least one spike to a brief, high-intensity pulse of blue light were included for analysis.

Optogenetic stimulation *in vitro*. Photostimulation of ChR2-expressing neurons was triggered by an Arduino UNO that sampled the membrane potential of the 'trigger' neuron in real time (10-kHz sampling). The threshold for spike detection was 0 mV. The blue light was generated using a multicolor LED light engine (Lumencor Spectra X) controlled by digital outputs (NI PCIe-6353) and was routed via a liquid light guide before being focused onto the slice chamber using a 40× objective lens. Light intensity was titrated to induce a single action potential in $ChR2^+$ SOM neurons to a 1-ms pulse of light. To impose simulated excitatory conductances (sEPSGs), a custom analog dynamic clamp was used[59]. The sEPSG waveforms were generated by convolving an EPSG-shaped template with a binary Poisson train.

Analysis of *in vitro* experiments. All analysis was performed using custom-written code or freely available packages (Chronux[60] in Matlab). Power spectra and phase locking were calculated as described for the *in vivo* data, with four leading tapers and a time–bandwidth product of 2. Charge was calculated as the integral of the EPSC/IPSC during photostimulation. Average values are expressed as mean ± s.e.m. Cells that exhibited peak gamma power lower than 25 pA^2/Hz were excluded from analysis.

Spike–spike coherence was computed as the power spectrum of a 300-ms window, centered at zero, of the cross-correlation between the spike trains of the recorded neurons. Spike-coupling, a metric of spike synchrony, was computed as the increase in spiking probability during a 5-ms window surrounding a zero time-lag between spikes. Interspike interval (ISI) histograms were computed with 4-ms time bins. Cross-spectra were computed as the spectral power of the cross-correlation between −100- and +100-ms lag times, giving a 6-Hz bin. Coherence was computed using a 250-ms Welch window. Synchronous spike counts were calculated as the number of spikes in the 'follower' cell during a 10 ms window surrounding a trigger cell spike.

Statistics. We used only nonparametric statistical tests (Kruskal-Wallis ANOVA, Wilcoxon signed-rank, rank-sum and Friedman tests) to determine significance except in **Supplementary Figure 6a**, where a two-factor design with interaction was needed. For this, the distribution was assumed to be normal, but this was not formally tested. No statistical methods were used to predetermine sample sizes. Visual stimulus presentation was randomized as outlined above. Data collection and analysis were not performed blind to the conditions of the experiments. A **Supplementary Methods Checklist** is available.

Computational modeling. The model consists of an excitatory population (E) and two inhibitory populations (I_{PV} and I_{SOM}) that capture the functional connectivity between pyramidal neurons, PV inhibitory neurons and SOM inhibitory neurons in the local network of layer 2/3 of the mouse visual cortex. The model defines the local network to be a group of neurons that code the same visual space and have similar tuning properties. The simplified firing rate model (equations 1–5) describes the temporal evolution of excitatory (r_E) and inhibitory ($r_{I_{PV}}$ and $r_{I_{SOM}}$) population firing rates of L2/3 neurons as a function of two types of external inputs ($i_{E_{L4}}$ and $i_{E_{L23}}$) to both the E and I populations. $i_{E_{L4}}$ is the input from excitatory population in L4; it is held constant during all the simulations included in this study to mimic the presence of an unchanging visual stimulus in the receptive field, i.e., the visual space coded by the local network (**Fig. 3b**). $i_{E_{L23}}$ is the input from the excitatory population of other local networks in L2/3 that code the visual space in the surround area and project their output through lateral connections. τ_E, $\tau_{I_{PV}}$ and $\tau_{I_{SOM}}$ indicate the rates at which the populations approach their steady state firing rates.

$$\tau \frac{dr_E}{dt} = -r_E + G_E\begin{pmatrix} W_{EE}\cdot r_E - W_{EI_{PV}}\cdot r_{I_{PV}} - W_{EI_{SOM}}\cdot r_{I_{SOM}} \\ +W_{EE_{L4}}\cdot i_{E_{L4}} + W_{EE_{L23}}\cdot i_{E_{L23}} \end{pmatrix} \quad (1)$$

$$\tau_{I_{SOM}} \frac{dr_{I_{SOM}}}{dt} = -r_{I_{SOM}} + G_{I_{SOM}}\begin{pmatrix} W_{I_{SOM}E}\cdot r_E - W_{I_{SOM}I_{PV}}\cdot r_{I_{PV}} - W_{I_{SOM}I_{SOM}}\cdot r_{I_{SOM}} \\ +W_{I_{SOM}E_{L4}}\cdot i_{E_{L4}} + W_{I_{SOM}E_{L23}}\cdot i_{E_{L23}} \end{pmatrix} \quad (2)$$

$$\tau_{I_{PV}} \frac{dr_{I_{PV}}}{dt} = -r_{I_{PV}} + G_{I_{PV}}\begin{pmatrix} W_{I_{PV}E}\cdot r_E - W_{I_{PV}I_{PV}}\cdot r_{I_{PV}} - W_{I_{PV}I_{SOM}}\cdot r_{I_{SOM}} \\ +W_{I_{PV}E_{L4}}\cdot i_{E_{L4}} + W_{I_{PV}E_{L23}}\cdot i_{E_{L23}} \end{pmatrix} \quad (3)$$

$$i_{E_{L4}} = \text{constant} \quad (4)$$

$$i_{E_{L23}} = \begin{cases} MIN_{i_{E_{L23}}} + (\text{surround\_size} - 1)\times m_{i_{E_{L23}}}, & \text{surround\_size} \geq 1 \\ 0, \text{ otherwise} \end{cases} \quad (5)$$

G_E, $G_{I_{PV}}$ and $G_{I_{SOM}}$ are the population response functions: they map the firing rates of the three neural populations in the local network as a function of their net inputs[39,61]. G_E and $G_{I_{SOM}}$ are described by threshold-linear functions, while $G_{I_{PV}}$ is described by a supralinear function of weighted inputs x to the respective subnetwork, as described in equations 6 and 7. The parameters m and θ describe the threshold input and rate of the response functions, respectively. Their values for the excitatory, PV and SOM populations in our model are defined in **Supplementary Table 1**.

$$G_E(x) = \begin{cases} 0 & \text{for} \quad x < \theta_E \\ m_E(x-\theta_E) & \text{for} \quad \theta_E < x < \theta_E + 1/m_E \\ 1 & \text{for} \quad x > \theta_E + 1/m_E \end{cases}$$

and

$$G_{I_{SOM}}(x) = \begin{cases} 0 & \text{for} \quad x < \theta_{I_{SOM}} \\ m_{I_{SOM}}(x-\theta_{I_{SOM}}) & \text{for} \quad \theta_{I_{SOM}} < x < \theta_{I_{SOM}} + 1/m_{I_{SOM}} \\ 1 & \text{for} \quad x > \theta_{I_{SOM}} + 1/m_{I_{SOM}} \end{cases} \quad (6)$$

$$G_{I_{PV}}(x) = \begin{cases} 0 & \text{for} \quad x < \theta_{I_{PV}} \\ m_{I_{PV}}(x-\theta_{I_{PV}})^3 & \\ 1 & \text{for} \quad G_{I_{PV}} > 1 \end{cases} \quad (7)$$

Previous work has shown that this choice of response functions results in network oscillations whose strength is positively correlated with the suppression of excitatory activity[27]. In the two-population model, this choice of response functions ensures an increase in the strength of oscillations either by increase in excitation to the I population or decrease in excitation to E population[26,27]. When extended to the current model, this choice of response functions predicts an increase in the strength of oscillations in response to either withdrawal of excitation to the E population or an increase in excitation to PV or SOM populations. $i_{E_{L23}}$ reflects the net response of the L2/3 excitatory populations that code for the surrounding visual space. In our model, this response is modeled as a linear function of the size of the surround visual stimulus (equation 5 and **Fig. 3b**), with the parameters as defined in **Supplementary Table 1**. For the results shown in **Figure 3** and **Supplementary Figure 5**, we varied the *surround_size* parameter from 1 to 4, in integer steps, to simulate increasing sizes of the visual surround. The steady-state firing rate of each population is determined by the weighted sum of individual population firing rates and the external input. All the weights (W_{XY}: from population Y to population X) are positive numbers representing strength of connections (**Supplementary Table 1**). For example, W_{EE} represents the product of the average number of recurrent excitatory contacts

doi:10.1038/nn.4562

per cell and the average postsynaptic current arising from one presynaptic action potential. The two inhibitory subpopulations are differentiated as SOM and PV based on the connections they form with each other and with the excitatory population, and also based on the relative strengths of inputs from L4 and L2/3 to each inhibitory population. Connectivity between the excitatory and PV inhibitory populations was tuned to keep the E–PV subnetwork in an inhibition-stabilized network (ISN) regime[62]. Previous modeling work has shown that the presence of surround-facilitation in SOM neurons[59] is compatible with the E–PV loop being in the ISN regime[63]. $W_{I_{SOM}I_{SOM}}$ reflects the evidence for weak connectivity between SOM neurons[28]. $W_{EE_{L23}}$ was set to zero, since the net effect of L2/3 lateral input in this model is inhibitory[59], through its action on mainly SOM neurons. Nonzero values of $W_{EE_{L23}}$ did not change the qualitative results as long as the net effect of lateral input was inhibitory in the local network. The steady-state network behavior is determined by the intersection of the $\frac{dr_E}{dt}=0$, $\frac{dr_{I_{SOM}}}{dt}=0$ and $\frac{dr_{I_{PV}}}{dt}=0$ curves in the ${}^{r}E{}^{r}I_{SOM}{}^{r}I_{PV}$ hyperplane.

Supplementary Table 1 shows the parameter values used for generating the simulation data. Given the values of time constants, the connection weights were chosen such that the frequency of the oscillations in the model was in the gamma range; more specifically, in the 20–30 Hz range. The model network was simulated using Matlab 2014b (Mathworks, Natick, MA). The power spectral density (PSD) of the average activity signal was estimated nonparametrically by calculating the discrete-time Fourier transform of the signal. Gamma power was reported as the peak power at the center frequency of the narrowband peak in the PSD in the 20–30 Hz range.

Code availability. All analysis and modeling code can be made available by the authors upon reasonable request.

Data availability. All relevant data for the experimental and theoretical work can be made available by the authors upon reasonable request.

51. Brainard, D.H. The psychophysics toolbox. *Spat. Vis.* **10**, 433–436 (1997).
52. Mitra, P. & Bokil, H. *Observed Brain Dynamics* (Oxford University Press, 2008).
53. Hill, D.N., Mehta, S.B. & Kleinfeld, D. Quality metrics to accompany spike sorting of extracellular signals. *J. Neurosci.* **31**, 8699–8705 (2011).
54. Muñoz, W., Tremblay, R. & Rudy, B. Channelrhodopsin-assisted patching: in vivo recording of genetically and morphologically identified neurons throughout the brain. *Cell Rep.* **9**, 2304–2316 (2014).
55. Ma, Y., Hu, H., Berrebi, A.S., Mathers, P.H. & Agmon, A. Distinct subtypes of somatostatin-containing neocortical interneurons revealed in transgenic mice. *J. Neurosci.* **26**, 5069–5082 (2006).
56. Pluta, S. *et al.* A direct translaminar inhibitory circuit tunes cortical output. *Nat. Neurosci.* **18**, 1631–1640 (2015).
57. Vinck, M., van Wingerden, M., Womelsdorf, T., Fries, P. & Pennartz, C.M. The pairwise phase consistency: a bias-free measure of rhythmic neuronal synchronization. *Neuroimage* **51**, 112–122 (2010).
58. Oostenveld, R., Fries, P., Maris, E. & Schoffelen, J.M. FieldTrip: open source software for advanced analysis of MEG, EEG, and invasive electrophysiological data. *Comput. Intel. Neurosc.* http://dx.doi.org/10.1155/2011/156869 (2011).
59. Adesnik, H. & Scanziani, M. Lateral competition for cortical space by layer-specific horizontal circuits. *Nature* **464**, 1155–1160 (2010).
60. Bokil, H., Andrews, P., Kulkarni, J.E., Mehta, S. & Mitra, P.P. Chronux: a platform for analyzing neural signals. *J. Neurosci. Methods* **192**, 146–151 (2010).
61. Ozeki, H., Finn, I.M., Schaffer, E.S., Miller, K.D. & Ferster, D. Inhibitory stabilization of the cortical network underlies visual surround suppression. *Neuron* **62**, 578–592 (2009).
62. Tsodyks, M.V., Skaggs, W.E., Sejnowski, T.J. & McNaughton, B.L. Paradoxical effects of external modulation of inhibitory interneurons. *J. Neurosci.* **17**, 4382–4388 (1997).
63. Litwin-Kumar, A., Rosenbaum, R. & Doiron, B. Inhibitory stabilization and visual coding in cortical circuits with multiple interneuron subtypes. *J. Neurophysiol.* **115**, 1399–1409 (2016).

Corrigendum: Cortical gamma band synchronization through somatostatin interneurons

Julia Veit, Richard Hakim, Monika P Jadi, Terrence J Sejnowski & Hillel Adesnik
***Nat. Neurosci.*; doi:10.1038/nn.4562; corrected online 16 June 2017**

In the version of this article initially published online, ref. 14 was given as Saleem, A. *et al.* On the origin and modulation of narrow-band gamma oscillations in mouse primary visual cortex. *Perception* **45**, abstr. 702 (2016). The correct reference is Saleem, A.B. *et al.* Subcortical source and modulation of the narrowband gamma oscillation in mouse visual cortex. *Neuron* **93**, 315–322 (2017). The error has been corrected in the print, PDF and HTML versions of this article.